Publications of the Astronomical Society of the Pacific, 132:034101 (16pp), 2020 March https://doi.org/10.1088/1538-3873/ab6714

The Multi-object Spectroscopy Observation of Seven Interacting Galaxy Pairs: Metallicity Gradients and Star Formation Distributions

Bing-qing Zhang[1,2], Chen Cao[3,4], Cong K. Xu[1,5], Zhi-min Zhou[1], and Hong Wu[1,2]
[1] National Astronomical Observatories, Chinese Academy of Sciences, 20A Datun Road, Chaoyang District, Beijing, 100101, People's Republic of China
bqzhang@bao.ac.cn
[2] School of Astronomy and Space Science, University of Chinese Academy of Sciences, Beijing 100049, People's Republic of China
[3] School of Space Science and Physics, Shandong University, Weihai, Shandong 264209, People's Republic of China; caochen@sdu.edu.cn
[4] Shandong Key Laboratory of Optical Astronomy & Solar-Terrestrial Environment, Institute of Space Sciences, Shandong University, Weihai, Shandong 264209, People's Republic of China
[5] Chinese Academy of Sciences South America Center for Astronomy, China-Chile Joint Center for Astronomy, Camino El Observatorio 1515, Las Condes, Santiago, Chile
Received 2019 September 10; accepted 2020 January 2; published 2020 January 28

Abstract

We use the Multi-Object Spectroscopy system of Xinglong 2.16 m telescope to study the gradients of gas-phase oxygen abundance and the distributions of star formation activities of seven nearby interacting galaxy pairs. On the basis of emission line luminosities and flux ratios, we estimate the gas-phase metallicities (log(O/H)), excitation mechanisms, and star formation rates (SFRs) of different regions in each galaxy. The average radial slope of log (O/H) from linear fitting of galaxy pairs in our sample is significantly flatter than that of isolated disk galaxies, also the central metallicity is much lower for interacting galaxies. This supports the predictions and results of previous theoretical numerical simulations and observational works which show the cold gas inflows induced by galaxy interactions can dilute the central metallicity. From the analysis of the radial distribution of SFR surface densities ($\Sigma_{\rm SFR}$), we find that, in our sample, galaxies in Spiral–Spiral (S+S) pairs have peak $\Sigma_{\rm SFR}$ at the center region and lower SFRs at the outer parts than that at the center. On the other hand, for two spirals in Spiral-Elliptical (S+E) pairs (Arp142 and J0338+2120), they both have relatively higher ($\Sigma_{\rm SFR}$) in their off-nuclei regions. This may hint a dependence of star formation distributions for paired galaxies on their companion morphologies.

Key words: galaxies: abundances – galaxies: evolution – galaxies: interactions – galaxies: star formation – HII regions – techniques: spectroscopic

Online material: color figures

1. Introduction

Galaxy interaction/merging is an important mechanism for galaxy evolution, affecting the morphology, star formation activities, and the growth of galaxies. Since Toomre & Toomre (1972) took a simulation and predicted that galaxy disks can be disturbed by galaxy interaction, a great amount of works about properties caused by merger (e.g., changes in morphology, star formation activity, and direction of evolution) and the relationship between these properties and galaxy interaction sprout. Theoretical and numerical simulations predict that the galaxy interaction causes the inner flow of the cold gas, flattening the gradient of the metallicity, at the same time trigging starburst over there (e.g., Barnes & Hernquist 1996; Mihos & Hernquist 1996; Kewley et al. 2006).

Galaxy interaction can lead to metallicity dilution. Previous observational studies have shown that the central metallicities of local galaxy close pairs and merging luminous infrared galaxies are lower than that of isolated galaxies of the same luminosity (e.g., Rupke et al. 2008, 2010; Kewley et al. 2010; Zhou et al. 2011). Similarly, the metallicity of galaxy pairs found in Sloan Digital Sky Survey (SDSS) is on average lower than isolated galaxies (Ellison et al. 2008; Michel-Dansac et al. 2008), suggesting that merger-induced gas-flows can flatten the central metallicity.

Galaxy interaction can lead to star formation activity enhancement (Kennicutt et al. 1987; Xu & Sulentic 1991). Many authors (e.g., Gavazzi & Jaffe 1985; Moss & Whittle 1993) have found that galaxies in cluster have statistical significantly enhanced star formation rate (SFR). Further works show star formation enhancement in interacting galaxy systems such as Arp24 (Cao & Wu 2007), NGC4485 & NGC4490 (Thronson et al. 1989), Arp30 (Kovo et al. 1996), and Arp86 (Zhou et al. 2014).

The star formation enhancement in different type of galaxy pairs is different. Using *Herschel Space Observatory*, *Wide-Field Infrared Survey Explorer*, and SDSS data, Cao et al. and Domingue et al. presented an analysis of 88 local close major-merger galaxy pairs (H-KPAIRs) and drew a conclusion that star-forming spiral galaxies in Spiral–Spiral (S+S) pairs show

significantly higher specific star formation rates (sSFRs) and star formation efficiencies (SFEs) than that in Spiral-Elliptical (S+E) pairs and isolated disk galaxies in the control sample. This confirms the previous result found by observations using *Spitzer Space Telescope* (Xu et al. 2010). The same H-KPAIRs sample was observed by Zuo et al. (2018) using the GBT 110 m telescope for the H I 21 cm line emission. They found that the star-forming galaxies (SFGs) in S+S and S+E pairs have about the same average H I gas fraction, while the average $SFE_{H\,I}$ (=$SFR/M_{H\,I}$) of SFGs in S+S pairs is 5 times higher than that of SFGs in S+E pairs.

Long-slit spectroscopic observations (e.g., Donzelli & Pastoriza 1997) can study many galaxy properties such as luminosity distribution, SFRs, relationship between interaction and active nuclei, and ages of the star formation events. More efficiently, the multi-object spectroscopic (MOS) observations can obtain several spectra of different regions in a target source simultaneously. Using an MOS, Zhou et al. (2014) have made a detailed study on the metallicity and star formation activities of H II regions in the interacting system Arp86, they measured fluxes of several emission lines and derived properties of dust extinction, excitation mechanism, radial distribution of metallicity, star formation, and stellar population. In the current study, we present a MOS observational study on a sample of seven local close major-merger galaxy pairs selected from our parent sample H-KPAIRs (Cao et al. 2016), as described in Section 2.1.

The rest of the paper is arranged as follows. Section 2 describes the sample selection, observed procedures and instruments, and data reduction procedures. Section 3 shows the results of our analysis on metallicity, star formation, and excitation mechanism. Discussions on the difference between S+S and S+E pairs are given in Section 4. Section 5 summarizes our work. Throughout this paper, we adopt the Λ-cosmology with $\Omega_m = 0.3$ and $\Omega_\Lambda = 0.7$, and $H_0 = 70$ (km s^{-1} Mpc^{-1}).

2. Sample, Observation and Data Reduction

2.1. Sample Selection

In the previous work, Domingue et al. and Xu et al. have built a *K*-band sample of 170 major-merger galaxy pairs (KPAIRs) by combining the Two Micron All Sky Survey (2MASS) with SDSS Data Release 5 (DR5) (Domingue et al. 2009; Xu et al. 2010, 2012). From KPAIR, Cao et al. (2016) selected 88 pairs (44 S+S and 44 S+E) and observed them with Hershel PACS and SPIRE, which constitute our parent sample H-KPAIR. From H-KPAIR, we select 7 pairs that are relatively large and bright, and have high sSFRs, to analyze the spatially resolved star formation and gas-phase metallicity properties. All spiral galaxies in these pairs have the SFR above the mean of the Main Sequence (Cao et al. 2016). Table 1 lists the pair name, R.A., decl., pair type (S+S or S+E), observing date, (on-target) exposure times, and grism used of our sample.

2.2. Observations

Our MOS observations were carried out using the MOS mode of the BAO faint object spectrograph and camera (BFOSC) system of the Xinglong 2.16 m telescope (Fan et al. 2016) of National Astronomical Observatories, CAS.[6] In each observation, we obtained several spectra simultaneously using a plate with pin holes (see Zhou et al. 2014 for detailed descriptions). The $f/9$ Cassegrain focus was used. Observations carried out before the year 2016 were using the E2V 55-30-1-348 CCD detector, with a pixel size of 22.5 × 22.5 μm, pixel scale of $0\farcs457$ pixel^{-1} and field of view (FoV) of $9\farcm46 \times 8\farcm77$, while those carried out after the year 2016 were using the new DZ936N-BEX2-DD-9TT-1 CCD detector, with a pixel size of 13.5 × 13.5 μm, pixel scale of $0\farcs274$ pixel^{-1} and FoV of $9\farcm36 \times 9\farcm36$. The dates of our observations are listed in Table 1.

Technical details of our MOS observations can be found in Zhou et al. (2014). Using the precise machine, we prepared a plate with holes according to the target coordinates for each observation. For the hole positions, we usually chose the nucleus of galaxy, bright knots (the areas of the tidal structure and overlap regions), and other areas that we were interested in. Figure 1 shows the SDSS images of the 7 pairs in our sample, with hole positions of our MOS observations marked on them. For all observations of science targets, the aperture of pinholes was $2\farcs2$.

In order to distinguish two spectra, it was required that two neighbor holes should be vertically (in the decl. direction) 5″ apart in space. For galaxy pairs J1602+4111 and Arp142, the grism we used was G7+385LP, with a spectral resolution of 2.13 Å per pixel, providing wavelength coverage of ∼3780–6760 Å. For the other pairs, the grism we used was G4+385LP, with a spectral resolution of 4.45 Å per pixel, providing wavelength coverage of ∼3600–8700 Å.

Followings are the procedures for our MOS observations: (1) First, bias, flat spectra, and Fe/Ar lamp spectra for wavelength calibrations were recorded. Noted that each pinhole plate needed their own flat spectra and Fe/Ar lamp spectra. We used flat lamp to illuminate the plate to obtain flat spectra; (2) second, we obtained several images adjusted by guide stars in the FoV to ensure that the hole plate was in the correct place; (3) Finally, we made MOS observations on the object and standard star. Note that for some targets we had two pinhole plates R & Y (red & yellow) with different regions. For the observation of standard stars, we used a plate with a series of holes with different diameters along its diagonal at five positions (see the bottom-right sub-panel in Figure 1). It shows that for every diameter, there are two same holes so that we would get double spectra. One of the two holes was used to get the standard star spectrum, another to get skylight

[6] Detailed description of BFOSC can be found at: http://www.xinglong-naoc.org/html/gcyq/216/detail-18.html.

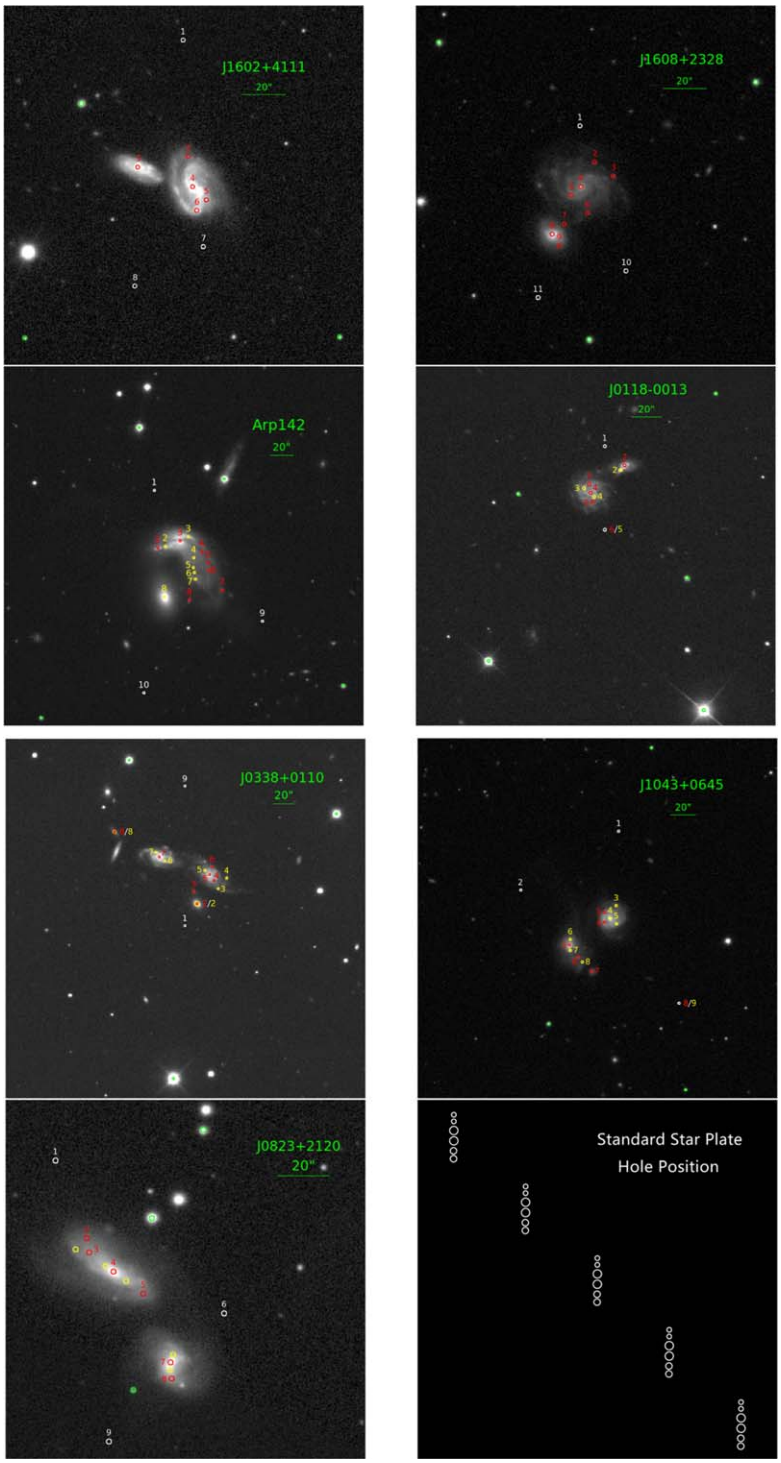

Figure 1. The hole position of seven galaxy pairs of our sample, background images are from SDSS. Red and yellow circles (represents two plates we used) on galaxies are the positions we observed; green circles denote the positions of guide stars, while white circles are pinholes used for sky subtraction. The sub-panel in the bottom-right corner shows the pinhole positions for observing the standard stars (for flux calibrations).
(A color version of this figure is available in the online journal.)

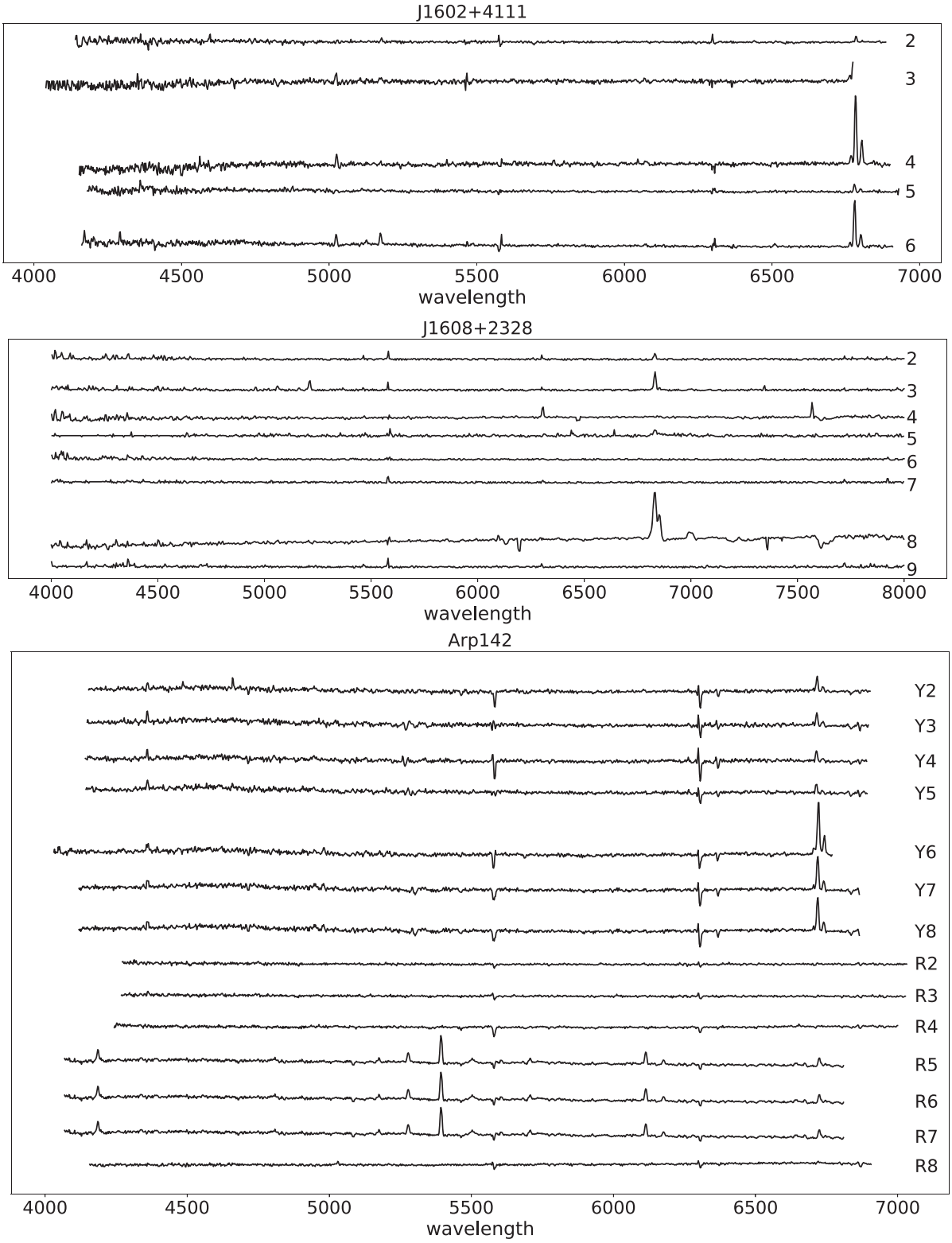

Figure 2. MOS spectra of galaxy pairs.

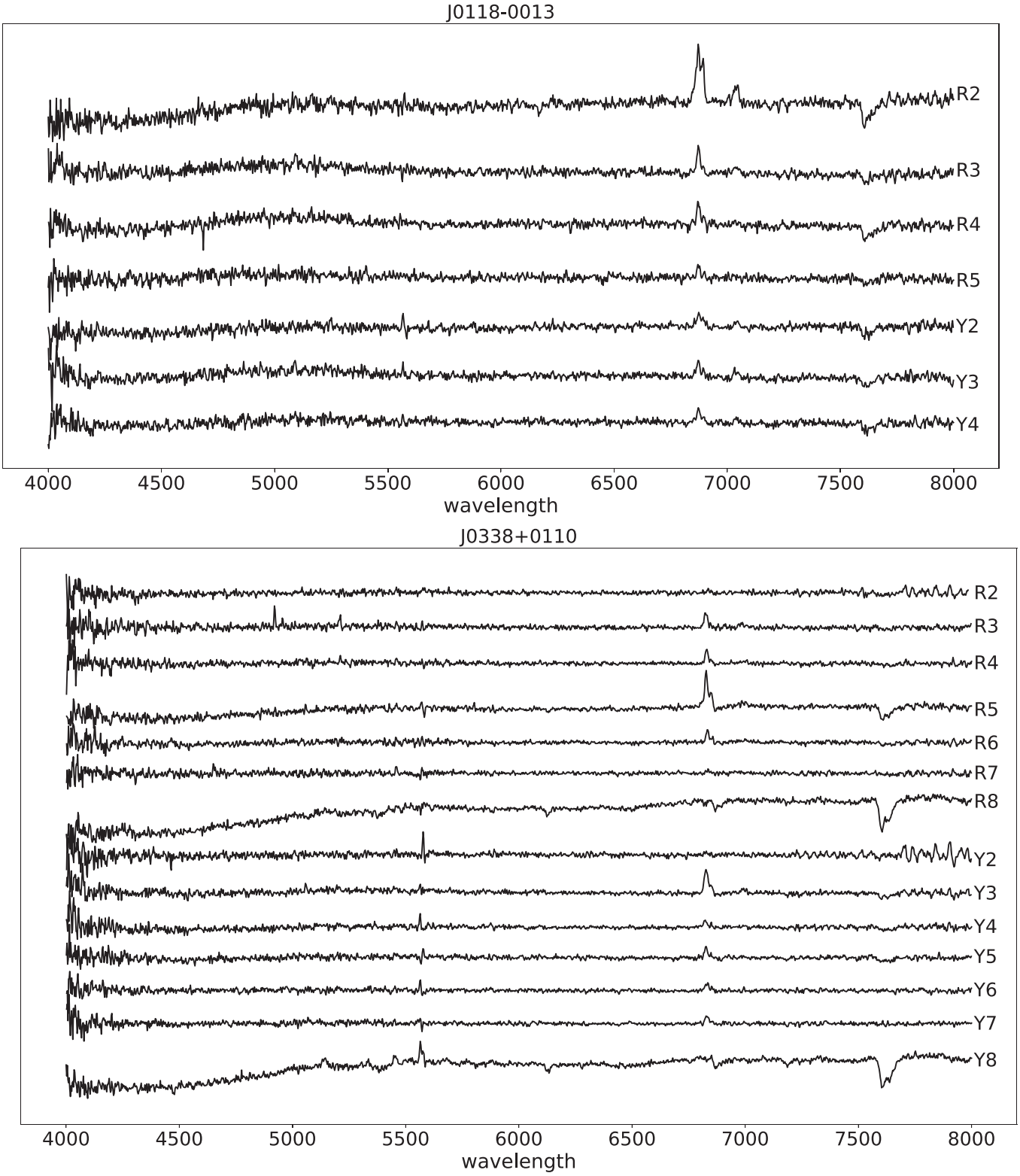

Figure 2. (Continued.)

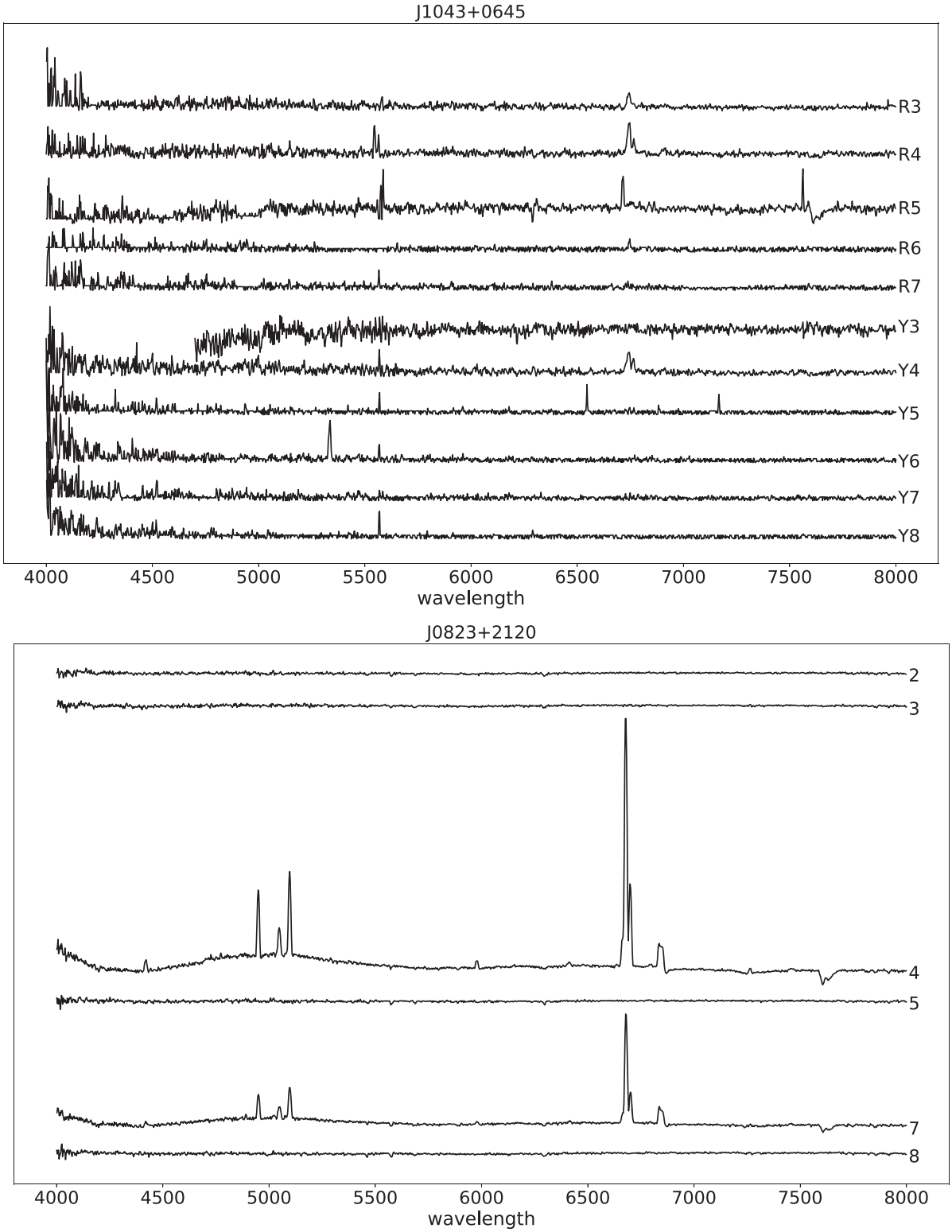

Figure 2. (Continued.)

Table 1
Sample and Observing Log

Galaxy Pair Name	R.A. (J2000.0)	Decl. (J2000.0)	Type	Observing Date (yyyy/mm/dd)	Exposure Times (s)	Grism
J1602+4111	16:02:42.58	+41:11:50.28	S+S	2014 Jul 26	3600 × 2	G7
J1608+2328	16:08:22.61	+23:28:45.84	S+S	2014 Jul 28	3600 × 2	G4
Arp142	09:37:44.14	+02:45:38.88	S+E	2015 Apr 24	3600	G7
J0118-0013	01:18:35.59	−00:13:59.16	S+S	2016 Nov 7	3600 × 2	G4
J0338+0110	03:38:12.22	+01:10:08.76	S+E (group)	2016 Nov 8	3600 × 2	G4
J0823+2120	08:23:34.20	+21:20:51.36	S+S	2017 Mar 18	3600 × 2	G4
J1043+0645	10:43:50.57	+06:45:46.80	S+S	2017 Mar 18	3600	G4

Note. Detail information of our sample.

(for sky background subtraction) simultaneously. We observed standard star at least on three positions to get a full wavelength coverage.

2.3. Data Reduction

We used the basic program of IRAF software to process our MOS data. The data reduction procedure includes bias subtraction, flat correction, cosmic ray removal, spectra extraction, wavelength calibration, flux calibration, and sky background subtraction. Compared with traditional long-slit spectroscopic observations, the data reduction of our MOS spectra was more complex and difficult because the wavelength coverage of each hole along the x (R.A.) direction was generally different, resulted from the spacial distribution. This also affected the sky background subtractions since the skylight hole might have different wavelength coverage than that of the object. Following is the pipeline of the BFOSC-MOS data reduction procedures:

1. Basic reduction. After bias subtraction, cosmic ray removal, and bad pixel removal, we extracted spectra of every hole and saved as one fits image. These include spectra of the target or the standard star, of the Iron Argon (FeAr) lamp, and of the flat. All were extracted using the same aperture that was derived empirically from the width of the flat spectrum in the 2D image of the flat taken with hole mask on. Then, flat correction was taken to eliminate the variances in the response and illumination.
2. Wavelength calibration. Based on the number of holes of one plate, wavelength calibration were done N times (N was the number of holes).
3. Flux calibration. We jointed several standard star spectra to obtain a full wavelength coverage spectrum.
4. Skylight subtraction. We averaged spectra of sky hole, and then this average sky spectrum was subtracted by the spectra of object.

3. Data Analysis and Results

3.1. Emission Line Measurements

After the MOS data reduction, we obtained several spectra for each object, which were then used for the subsequent analysis. Figure 2 shows all spectra we got. They all start at 4000 Å because the signal-to-noise ratio (S/N) of the blue end is too low, and for galaxy pairs who use G4 grism, the spectra after 8000 Å are not shown because there are no emission lines that we cared about. We made a single Gaussian fitting on each emission line to measure the flux, using python "lmfit" package. Figure 3 shows an example of spectrum fitting. A model of a single Gauss profile plus a straight line with slope was used to fit the emission line and small-range continumm level. The predicted central wavelength of an emission line, derived by the redshift of each galaxy pair, was used as the initial center of Gaussian profile. The initial values of other two parameters of Gaussian profile, amplitude and sigma, were set to the same order of magnitude as the emission line's peak values. All detected emission lines have S/Ns >3. Table 2 shows the emission line fluxes for each spectrum (the flux units are in 10^{-16} erg s^{-1} cm^{-2}), also the gas-phase metallicity (12+log (O/H)) and $\Sigma_{\rm SFR}$ as defined in Section 3. Numbers in blankets in Table 2 are errors.

3.2. BPT Diagram

In order to check the gas excitation mechanism for different regions in the pairs, we draw the "BPT" diagnostic diagram (Baldwin et al. 1981) in Figure 4. The horizontal axis is the emission line ratio of [N II]λ6583 and Hα, the vertical axis is the emission line ratio of [O III]λ5007 and Hβ. The solid line represents the maximum starburst line from Kewley et al. (2001) and the dashed line represents the pure star-forming line from Kauffmann et al. (2003).

Most of the regions we observed are under the pure star-forming line (dashed line in Figure 4), represent that the primary excitation mechanism is star formation, denoted as "SF" in Table 2. There is only one region in pair J1043+0645 (in magenta color) lies above the maximum starburst line (solid

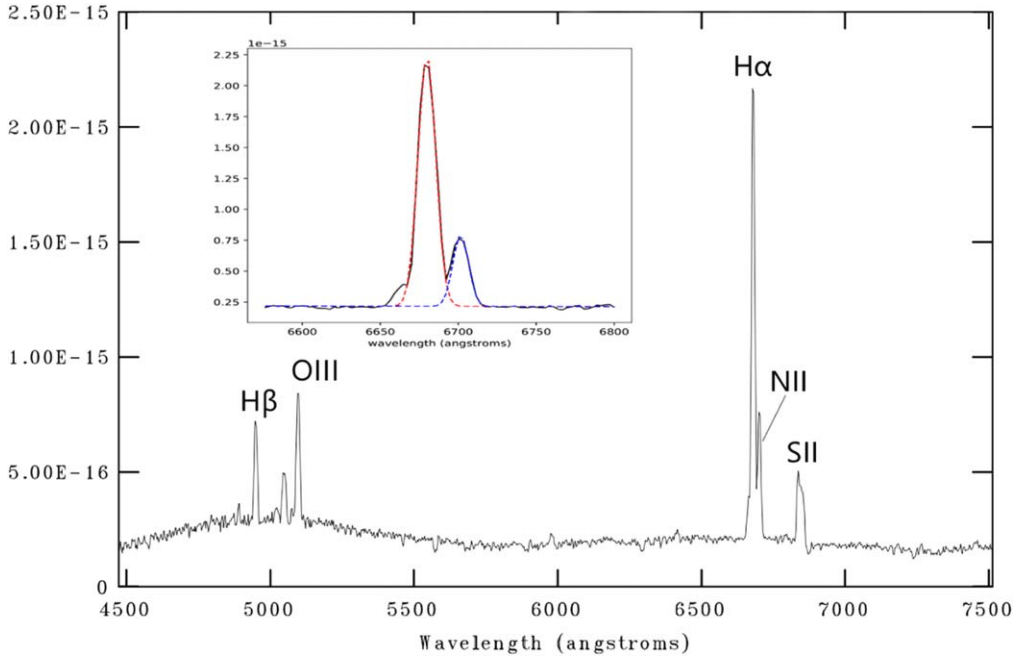

Figure 3. The spectrum of KPAIR J0823+2120 aperture 7. The sub-panel shows profiles of multi-component Gaussian line fitting. The red line and blue line are the fitting profiles of Hα and N II, respectively.
(A color version of this figure is available in the online journal.)

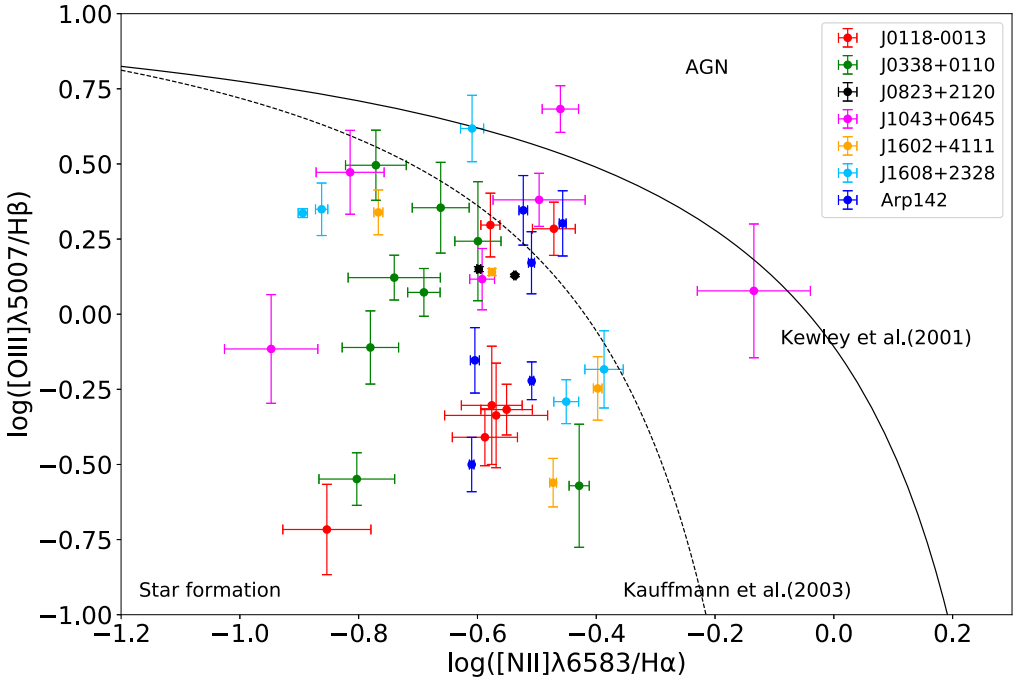

Figure 4. The BPT diagram with two demarcation. The solid line represents the maximum starburst line from Kewley et al. (2001) and the dashed line represents the pure star-forming line from Kauffmann et al. (2003). Different colors represent different galaxy pairs.
(A color version of this figure is available in the online journal.)

Table 2
Flux and Parameter

Name	Region ID[a]	R.A. (J2000.0)	Decl. (J2000.0)	Hβ λ4862	O III λ5007	Hα λ6563	Hα_corr[b] λ6563	N II λ6583	12+log (O/H)	Σ_{SFR}[c] ($M_\odot$ yr^{-1} kpc^{-2})	BPT-class[d]
J1602+4111	2	16:02:42.76	+41:12:03.78	5.692 (0.778)	12.419 (1.289)	21.943 (0.185)	47.177(16.786)	3.753 (0.057)	8.463 (0.004)	0.006(0.00047)	SF
	3	16:02:44.78	+41:11:58.93	31.053 (2.919)	24.839 (3.491)	…	…	…	…	…	…
	4	16:02:42.57	+41:11:50.10	32.158 (4.048)	8.845 (1.209)	283.319 (1.883)	5196.435 (1701.368)	95.434 (1.089)	8.631 (0.003)	0.665(0.048)	SF
	5	16:02:42.03	+41:11:43.97	0.936 (0.179)	0.53(0.08)	28.625 (0.205)	13244.637 (6567.36)	11.46 (0.172)	8.673 (0.004)	1.695(0.186)	SF
	6	16:02:42.40	+41:11:39.33	34.05 (0.784)	47.04 (0.643)	187.969 (1.096)	1025.503(64.933)	49.939 (0.506)	8.572 (0.003)	0.131(0.0018)	SF
J1608+2328	2	16:08:22.15	+23:28:57.17	5.539 (0.904)	12.374 (1.455)	52.943 (0.488)	1199.643 (509.344)	7.269 (0.159)	8.408 (0.006)	0.154(0.031)	SF
	3	16:08:21.53	+23:28:50.87	32.794 (0.982)	71.146 (1.126)	143.829 (1.149)	432.064(35.762)	18.359 (0.296)	8.39 (0.004)	0.055(0.002)	SF
	4	16:08:22.61	+23:28:45.98	1.014 (0.165)	4.207(0.82)	23.595(0.6)	5372.395 (2326.461)	5.804 (0.214)	8.553 (0.011)	0.688(0.142)	composite
	5	16:08:22.94	+23:28:42.02	17.448 (3.871)	11.433 (2.24)	64.767 (2.751)	126.232(75.15)	26.578 (1.622)	8.68 (0.018)	0.016(0.0046)	SF
	6	16:08:22.39	+23:28:34.07	…	…	…	…	…	…	…	…
	7	16:08:23.16	+23:28:29.08	…	…	…	…	…	…	…	…
	8	16:08:23.56	+23:28:24.45	18.864 (2.217)	9.652 (1.162)	593.667 (17.704)	295892.813 (95622.8)	210.376 (7.973)	8.643 (0.012)	37.877(5.84)	SF
	9	16:08:23.33	+23:28:19.17	6.712 (1.913)	6.865(1.43)	…	…	…	…	…	…
Arp142	Y2	09:37:44.98	+02:45:34.22	114.49 (15.429)	36.187 (5.737)	1040.349 (4.495)	20674.109 (7233.446)	255.542 (1.987)	8.552 (0.002)	2.646(0.057)	SF
	Y3	09:37:43.66	+02:45:42.32	142.306 (13.14)	85.454 (9.507)	1657.142 (6.053)	62664.653 (15030.999)	513.723 (3.539)	8.61 (0.002)	8.022(0.119)	SF
	Y4	09:37:43.33	+02:45:24.53	63.96 (11.92)	44.908 (7.524)	237.293 (2.003)	461.822(223.677)	59.016 (0.899)	8.556 (0.004)	0.059(0.0018)	SF
	Y5	09:37:43.38	+02:45:15.89	32.121 (6.154)	71.185 (13.192)	282.992 (2.029)	5190.497 (2582.736)	84.905 (1.275)	8.602 (0.004)	0.664(0.02)	composite
	Y6	09:37:43.29	+02:45:11.38	45.394 (7.96)	91.035 (16.211)	350.456 (2.329)	4563.669 (2078.594)	122.507 (1.398)	8.64 (0.003)	0.584(0.016)	composite
	Y7	09:37:43.24	+02:45:05.89	14.428 (2.658)	21.4(3.221)	393.997 (2.298)	135909.329 (65012.921)	122.032 (1.237)	8.61 (0.003)	17.398(0.51)	SF
	Y8	09:37:45.04	+02:44:50.74	…	…	…	…	…	…	…	…
	R2	09:37:45.44	+02:45:33.10	…	29.495 (5.898)	45.368 (3.873)	45.368(0.0)	12.196 (1.361)	8.575 (0.035)	0.006(0.0)	…
	R3	09:37:44.12	+02:45:39.22	13.688 (1.805)	…	251.486 (6.775)	31035.003 (11033.32)	49.841 (2.899)	8.499 (0.016)	3.973(0.087)	…
	R4	09:37:42.86	+02:45:29.70	…	…	19.849 (3.507)	19.849(0.0)	8.581 (1.466)	8.692 (0.061)	0.003(0.0)	…
	R5	09:37:42.51	+02:45:20.26	…	…	17.525 (3.537)	17.525(0.0)	11.817 (3.018)	8.802 (0.081)	0.002(0.0)	…

Table 2
(Continued)

Name	Region ID[a]	R.A. (J2000.0)	Decl. (J2000.0)	Hβ λ4862	O III λ5007	Hα λ6563	Hα_corr[b] λ6563	N II λ6583	12+log (O/H)	Σ_{SFR}[c] ($M_\odot$ yr^{-1} kpc^{-2})	BPT-class[d]
	R6	09:37:42.47	+02:45:13.56	…	…	23.939 (3.25)	23.939(0.0)	…	…	0.003(0.0)	…
	R7	09:37:41.67	+02:44:56.25	…	…	…	…	…	…	…	…
	R8	09:37:43.60	+02:44:47.64	…	…	9.375 (1.645)	9.375(0.0)	…	…	0.001(0.0)	…
J0118-0013	R2	01:18:34.12	−00:13:41.70	60.756 (11.031)	120.291 (19.631)	856.366 (13.115)	53141.589 (25197.355)	226.171 (7.604)	8.57 (0.009)	6.803(3.19)	SF
	R3	01:18:35.65	−00:13:53.93	108.742 (13.045)	20.892 (6.78)	265.199 (8.802)	265.199(0.0)	37.158 (6.225)	8.413 (0.042)	0.034(0.0)	SF
	R4	01:18:35.60	−00:13:59.72	80.251 (16.05)	39.917 (16.229)	229.369 (8.916)	229.369(0.0)	60.905 (6.776)	8.572 (0.029)	0.029(0.0)	SF
	R5	01:18:35.51	−00:14:05.68	25.85 (4.418)	11.904 (4.311)	126.222 (9.366)	500.917(259.116)	34.084 (6.317)	8.576 (0.049)	0.064(0.033)	SF
	Y2	01:18:34.30	−00:13:44.76	29.576 (4.602)	56.908 (7.505)	182.978 (6.082)	1341.581 (564.604)	61.813 (4.704)	8.631 (0.021)	0.172(0.07)	composite
	Y3	01:18:35.88	−00:13:56.51	72.857 (7.476)	35.074 (5.786)	172.582 (6.541)	172.582(0.0)	48.541 (4.482)	8.586 (0.025)	0.022(0.0)	SF
	Y4	01:18:35.44	−00:14:02.30	71.188 (11.287)	27.725 (4.139)	164.004 (6.76)	164.004(0.0)	42.402 (5.061)	8.565 (0.031)	0.021(0.0)	SF
J0338+0110	R2	03:38:12.99	+01:09:41.37	2.794 (0.688)	13.613 (1.773)	21.598 (2.905)	282.232(226.188)	6.599 (2.018)	8.606 (0.083)	0.036(0.015)	SF
	R3	03:38:13.19	+01:09:52.78	10.915 (5.045)	59.605 (10.029)	163.559 (4.9)	11894.981 (14318.651)	13.532 (2.601)	8.283 (0.048)	1.523(0.965)	SF
	R4	03:38:11.92	+01:10:02.92	21.825 (2.983)	28.884 (2.997)	129.654 (18.634)	855.587(535.995)	23.588 (2.506)	8.478 (0.044)	0.11(0.036)	SF
	R5	03:38:12.21	+01:10:08.70	24.715 (3.728)	6.638 (2.966)	345.343 (5.142)	20950.789 (8272.31)	128.683 (4.647)	8.656 (0.01)	2.682(0.558)	SF
	R6	03:38:12.05	+01:10:16.23	11.392 (3.342)	19.928 (6.958)	116.632 (3.142)	3158.036 (2422.536)	29.35 (2.506)	8.558 (0.022)	0.404(0.163)	SF
	R7	03:38:15.38	+01:10:25.38	…	18.243 (4.378)	…	…	…	…	…	…
	R8	03:38:18.20	+01:10:49.34	…	…	…	…	…	…	…	…
	Y2	03:38:12.99	+01:09:41.40	…	…	16.403 (2.371)	16.403(0.0)	11.958 (1.293)	8.822 (0.045)	0.002(0.0)	SF
	Y3	03:38:11.65	+01:09:55.48	40.887 (4.122)	48.326 (7.382)	298.597 (5.272)	3366.335 (905.816)	60.943 (3.678)	8.507 (0.016)	0.431(0.061)	SF
	Y4	03:38:11.13	+01:10:05.68	5.086 (1.476)	11.5(2.203)	82.951 (3.617)	7514.37 (5775.741)	18.069 (1.832)	8.523 (0.027)	0.962(0.389)	composite
	Y5	03:38:12.48	+01:10:12.74	22.434 (5.516)	17.384 (2.343)	109.46 (3.263)	433.55(280.36)	18.155 (1.91)	8.455 (0.027)	0.055(0.0189)	SF
	Y6	03:38:15.03	+01:10:21.69	8.037 (1.542)	25.166 (4.728)	92.248 (3.481)	3359.638 (1733.323)	15.631 (1.744)	8.461 (0.029)	0.43(0.117)	SF
	Y7	03:38:15.56	+01:10:29.89	38.062 (4.037)	10.763 (1.844)	93.981 (3.172)	93.981(0.0)	14.789 (2.112)	8.442 (0.036)	0.012(0.0)	SF
	Y8	03:38:18.20	+01:10:49.36	…	…	…	…	…	…	…	…

Table 2
(Continued)

Name	Region ID[a]	R.A. (J2000.0)	Decl. (J2000.0)	Hβ λ4862	O III λ5007	Hα λ6563	Hα_corr[b] λ6563	N II λ6583	12+log (O/H)	Σ_{SFR}[c] ($M_\odot$ yr^{-1} kpc^{-2})	BPT-class[d]
J1043+0645	R3	10:43:50.88	+06:45:51.50	8.497 (2.438)	25.2(3.642)	270.389 (7.299)	138703.174 (104106.606)	41.46 (5.348)	8.436 (0.033)	17.755(1.32)	SF
	R4	10:43:50.86	+06:45:43.73	67.373 (12.556)	88.13 (12.598)	591.042 (9.526)	10720.8589 (5219.362)	151.181 (6.853)	8.562 (0.012)	1.372(0.066)	SF
	R5	10:43:52.68	+06:45:25.79	31.447 (10.773)	24.095 (5.71)	359.015 (9.131)	12896.209 (11519.074)	40.529 (7.258)	8.36 (0.045)	1.651(0.146)	SF
	R6	10:43:52.21	+06:45:16.40	24.414 (4.212)	58.63 (6.301)	129.11 (7.509)	630.136(311.238)	41.19 (6.954)	8.617 (0.044)	0.081(0.004)	composite
	R7	10:43:51.50	+06:45:05.02	…	…	…	…	…	…	…	…
	Y3	10:43:50.22	+06:45:56.58	…	…	…	…	…	…	…	…
	Y4	10:43:50.55	+06:45:46.83	147.868 (26.332)	712.126 (11.329)	450.969 (14.252)	527.955(251.123)	156.234 (9.835)	8.638 (0.017)	0.068(0.003)	AGN
	Y5	10:43:50.22	+06:45:42.67	35.962 (17.305)	43.0(7.582)	47.411 (6.234)	47.411(0.0)	34.775 (6.098)	8.823 (0.054)	0.006(0.0)	composite
	Y6	10:43:52.64	+06:45:30.34	…	…	…	…	…	…	…	…
	Y7	10:43:52.65	+06:45:21.59	…	…	…	…	…	…	…	…
	Y8	10:43:52.03	+06:45:12.31	…	…	…	…	…	…	…	…
J0823+2120	2	08:23:34.94	+21:21:04.16	…	…	…	…	…	…	…	…
	3	08:23:34.87	+21:20:58.75	8.139 (1.855)	14.18 (4.124)	…	…	…	…	…	…
	4	08:23:34.22	+21:20:51.56	1601.694 (12.139)	2155.624 (11.887)	6652.545 (11.248)	17352.125 (357.038)	1931.791 (7.192)	8.594 (0.001)	2.221(0.00089)	SF
	5	08:23:33.42	+21:20:43.15	…	…	…	…	…	…	…	…
	7	08:23:32.67	+21:20:17.15	627.26 (9.892)	886.24 (9.509)	2883.543 (7.715)	9785.877 (411.187)	728.154 (5.016)	8.559 (0.002)	1.253(0.001)	SF
	8	08:23:32.64	+21:20:11.01	…	…	…	…	…	…	…	…

Notes. Line fluxes are in the unit of 10^{-16} erg s^{-1} cm^{-2}.
[a] Here capital letters "Y" and "R" respectively represent color "yellow" and "red," which corresponds to the color of the pictures in Figure 1.
[b] For some holes, errors of Hα_corr flux equal to 0 means we have not done any correction. One reason is that we have Hα flux but we have no Hβ flux, another reason is that the $E(B-V)$ we got is a negative number ($(H\alpha/H\beta)_{obs}/(H\alpha/H\beta)_{int} < 0$).
[c] For the holes who have no error of Hα_corr flux, we cannot get error of Σ_{SFR}.
[d] "SF" stands for star formation excitation, "AGN" stands for active galactic nuclei excitation, and "composite" stands for both star formation and AGN excitation.

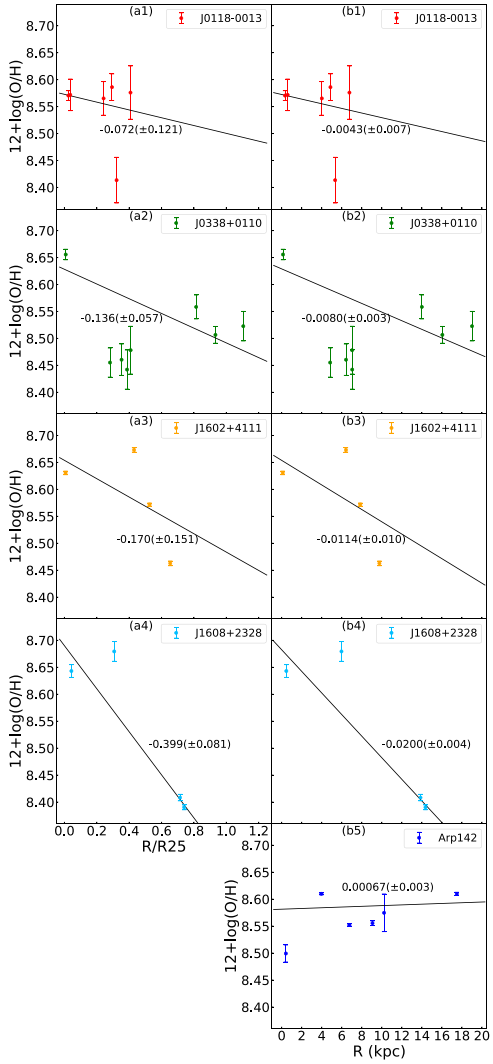

Figure 5. Radial distributions of the metallicity in galaxies with more than 4 data points. On the left column, the horizontal axis is the relative distance of the regions to the center of host galaxy, which is normalized by R25 measured by us, where R25 is the *B*-band isophote at a surface brightness of 25 mag arcsec^{-2}. On the right column, the horizontal axis is the physical distance in units of kiloparsecs. The symbols are the same as in Figure 4. The black line in these pictures represents the optimum linear fit for the scatters.

(A color version of this figure is available in the online journal.)

line in Figure 4), which is located at the center of the northwest galaxy (SDSS J10435053+0645466) of the pair, indicating possible (low level) active galactic nuclei (AGN) contribution, we denoted it as "AGN" in Table 2. For the other regions lying between the two lines, they are possibly excited by both star formation and AGN, or by shock (Kewley et al. 2001). They were denoted as "composite" in Table 2.

3.3. Gas-phase Metallicity Gradients

We use the $N2 = \log([\mathrm{N\,II}]\lambda6583/\mathrm{H}\alpha)$ index (PP04 N2) to estimate the gas-phase metallicity ($12 + \log(\mathrm{O/H})$) of H II regions in interacting system. Note that regions located above the pure star formation line (diagnostic line by Kauffmann et al. 2003, also shown as dashed line in Figure 4) in the BPT diagram (denoted as "composite" or "AGN" in Table 2) are excluded in the following analysis on the metallicity gradients, because the N2 index is sensitive to AGN's ionizing radiation. There are many researches about N2 index—a very useful indicator of gas-phase metallicities in SFGs (e.g., Storchi-Bergmann et al. 1994; Raimann et al. 2000; Denicoló et al. 2002; Liang et al. 2006; Marino et al. 2013). The formula to estimate the oxygen abundance in this work is $12 + \log(\mathrm{O/H}) = 8.9 + 0.57 \times \mathrm{N2}$ (Pettini & Pagel 2004). The gas-phase oxygen metallicities (12+log(O/H)) of each region are shown in Table 2.

In Figure 5, we show the radial distributions of gas-phase oxygen abundance (12+log(O/H)) of our galaxies. On the left column, the horizontal axis is the de-projected distance of the regions to the center of host galaxy, which is normalized by R25 measured by us, where R25 is radius of the *B*-band isophote at a surface brightness of 25 mag arcsec^{-2}. On the right column, the horizontal axis is the physical distance in units of kiloparsecs. Note that we did projection correction except for Arp142 because the SFG in this pair has extremely irregular morphology, which makes it very difficult to define the inclination and position angle. We excluded galaxies in J0823+2120 and J1043+0645 because either of them has less than 4 points to make a meaningful linear fitting. In subgraphs (a) and (b) of Figure 6, we plot metallicity versus relative distance and physical distance using all SF regions in the seven galaxy pairs. Most of the 12+log(O/H) values are between 8.3 and 8.7. The black line is the best linear fit for the 12+log(O/H) versus $R/R25$, using all SF regions in the seven galaxy pairs. The linear fitting function is: $12 + \log(\mathrm{O/H}) = 8.594(\pm0.009) - 0.137(\pm0.035)R/R_{25}$, corresponding to a gradient of approximately $-0.009(\pm0.002)$ dex kpc^{-1}.

In subgraphs (c) and (d) of Figure 6, we plot metallicity gradients for both interacting galaxies and isolated galaxies in our work and literatures. Solid lines denote the metallicity gradients of isolated spirals M101 (Kennicutt et al. 2003), and the average of isolated spiral galaxies studied in Rupke et al. (2010), while dashed lines denote that of our four interacting galaxies (in different colors), the interacting galaxy Arp86 (Zhou et al. 2014), the average of 16 interacting galaxies studied by Rupke et al. (2010), and the average of 8 galaxies in close pairs studied by Kewley et al. (2010). Since the methods used to calculate metallicity vary from paper to paper, we did not use the original results of the previous works in the above comparisons. Instead, we converted them to values corresponding to metallicities based on the same PP04(N2) method, which was used in this work and by Zhou et al. (2014). In Zhou et al. (2014), the interacting system Arp86 presents very flat metallicity gradient -0.09 dex R_{25}^{-1}, about -0.005 dex kpc^{-1}. In Kennicutt et al. (2003), they used the most direct method, the electron temperature (Te) indicator, to calculate metallicity,

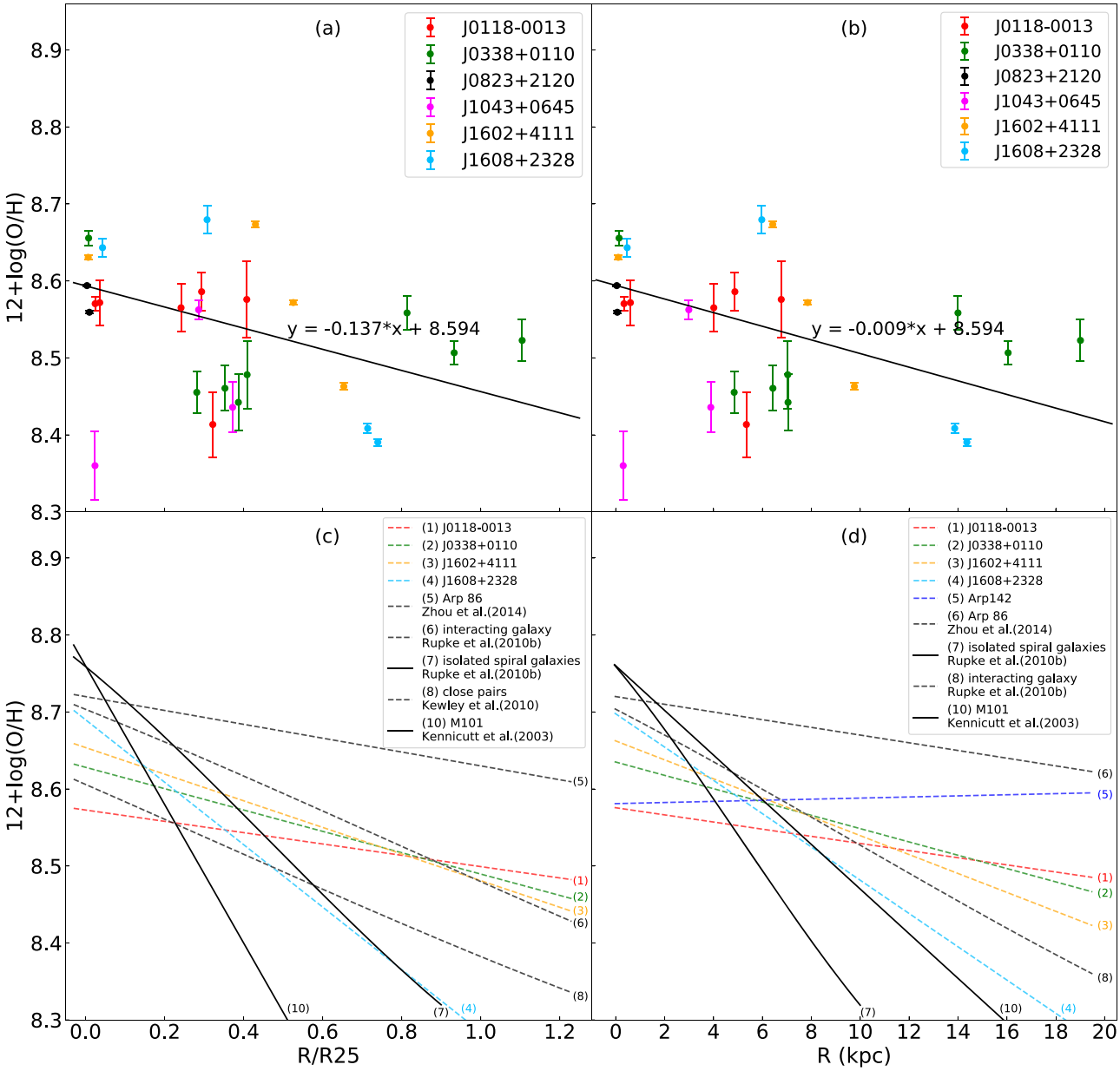

Figure 6. Metallicity in relation to relative distance (subgraph (a)) and physical distance (subgraph (b)) using all SF regions in the seven galaxy pairs. The symbols are the same as in Figure 4. The black line in these pictures represents the optimum linear fit for the scatters. Subgraph (c) and (d) compare the metallicity gradients between interacting galaxies and isolated galaxies. Dashed lines represent metallicity distribution of interacting galaxies, while solid lines represent that of isolated galaxies.

(A color version of this figure is available in the online journal.)

so we do not need to convert their results. The metallicity gradient of isolated galaxy M101 is -0.90 dex R_{25}^{-1}, about -0.029 dex kpc^{-1}. In Rupke et al. (2010) and Kewley et al. (2010), they both used KD02 indicator, so we transferred their results by applying the conversion factors in Kewley & Ellison (2008). These conversions changed the metallicity gradients taken from these papers from straight lines into curves (lines (6) and (7) and (8) in subgraph (c) and lines (7) and (8) in subgraph (d)).

From Figure 6 we find that the radial slope of log(O/H) from linear fitting for galaxy pairs in our sample is significantly flatter than that of isolated disk galaxies, also the central metallicity of the former is lower than that of the latter. This main result of our study support the prediction of previous

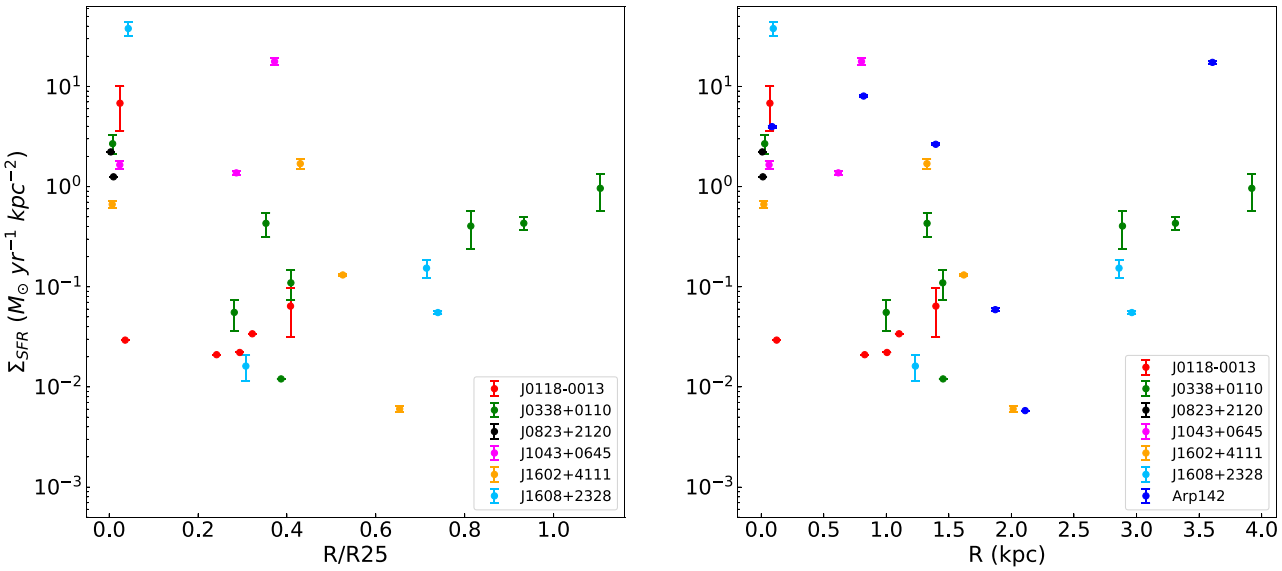

Figure 7. Left: Star formation rate surface densities ($\Sigma_{\rm SFR}$) vs. relative radius (R/R25) normalized by the isophotal radius at 25 mag arcsec^{-2} in the *B*-band for regions in our pairs except Arp142. Right: $\Sigma_{\rm SFR}$ vs. physical distance (kpc) for regions in our pairs. The symbols are the same as in Figure 4.
(A color version of this figure is available in the online journal.)

theoretical numerical simulations that interaction between galaxies can cause an inflow of outer cold gas so that the gas-phase metallicity gradient of galaxy is flattened and the central metallicity is diluted (Ellison et al. 2008; Michel-Dansac et al. 2008).

3.4. Star Formation Distributions

3.4.1. Hα Dust-correction

At first, the $L(\mathrm{H}\alpha)$ is corrected for internal dust extinction by using the "balmer decrement" method. The formula is derived from Calzetti (2001):

$$E(B-V) = 2.5\,\frac{\log[(\mathrm{H}\alpha/\mathrm{H}\beta)_{\rm obs}/(\mathrm{H}\alpha/\mathrm{H}\beta)_{\rm int}]}{R_{\mathrm{H}\beta} - R_{\mathrm{H}\alpha}} \quad (1)$$

$$A_{\mathrm{H}\alpha} = R_{\mathrm{H}\alpha} \times E(B-V) \quad (2)$$

$$L(\mathrm{H}\alpha)_{\rm obs} = L(\mathrm{H}\alpha)_{\rm corr} \times 10^{-0.4A_{\mathrm{H}\alpha}} \quad (3)$$

We assumed the applicability of the Calzetti et al. extinction law, parameterized by $R_{\mathrm{H}\alpha} = 3.32$, $R_{\mathrm{H}\beta} = 4.60$. An intrinsic $\mathrm{H}\alpha/\mathrm{H}\beta$ ratio of 2.87 was assumed from Case B recombination at 10^4 K (Osterbrock 1989). Both measured line fluxes (Hα) and dust-corrected values (Hα_corr) are shown in Table 2.

3.4.2. Star Formation Rates

There are two very distinct physical environments that large-scale star formation could take place in: one in compact dense centers of galaxies, another in the extended disks of spiral and irregular galaxies. The highest SFRs are associated almost uniquely with strong interactions and mergers (Kennicutt 1998). We used the dust-corrected Hα emission line luminosities (L(Hα_corr)) to estimate the SFRs for regions in our interacting galaxy pairs, the formula is from Kennicutt (1998):

$$\mathrm{SFR}_{\mathrm{H}\alpha}(M_\odot\ \mathrm{yr}^{-1}) = 7.9 \times 10^{-42}[L(\mathrm{H}\alpha\_\mathrm{corr})](\mathrm{erg\ s}^{-1}). \quad (4)$$

The values of SFR surface density $\Sigma_{\rm SFR}$ of each observed region are shown in Table 2. And the $\Sigma_{\rm SFR}$ was calculated using the formula:

$$\Sigma_{\rm SFR}(M_\odot\ \mathrm{yr}^{-1}\ \mathrm{kpc}^{-2}) = \frac{\mathrm{SFR}_{\mathrm{H}\alpha}(M_\odot\ \mathrm{yr}^{-1})}{S_{\rm hole}(\mathrm{kpc}^2)}. \quad (5)$$

The $S_{\rm hole}$ here is the physical area in the sky of the hole.

Figure 7 shows the distribution of SFR surface densities of our seven galaxy pairs. Most pairs have higher $\Sigma_{\rm SFR}$ at galaxy centers, and the value of $\Sigma_{\rm SFR}$ generally declines inside-out. This suggests that in interacting galaxies, a large amount of star formation occurs in the nuclear and circumnuclear regions, due to massive gas inflows induced by the interacting process. On the other hand, galaxy pairs Arp142 and J0338+2120 have relatively higher $\Sigma_{\rm SFR}$ at their outskirts, and for Arp142, the highest star formation does not locate at the center of the spiral galaxy. Interestingly, both Arp142 and J0338+2120 are classified as S+E pairs (J0338+2120 is in a small group).

4. Discussion: Differences between S+S and S+E Pairs

Of the seven galaxy pairs we studied in this work, only two pairs (Arp142 and J0338+2120) are Spiral-Elliptical (S+E) systems, others are all Spiral–Spiral (S+S) pairs. From the above analysis on gas-phase metallicity gradients and the radial

distribution of SFR surface densities (see Figures 5–7), we found that the log(O/H) and Σ_{SFR} profiles for Arp142 and J0338+2120 are all flatter than other spirals in S+S pairs. Although our sample is too small to make a firm conclusion, this result might suggest that star formation activities, as well as cold gas with lower metallicity, occur not only in the nuclear region but also in off-nuclei areas of the spiral galaxy in S+E pairs. On the other hand, for spirals in S+S pairs, enhanced star formation and inflow gas are more likely to be found in the very center. Off-nuclei star formation and young massive super star clusters are found in some previous studies on nearby interacting galaxies (e.g., Cao & Wu 2007; Smith et al. 2014, 2016) and simulated major mergers (Powell et al. 2013). In addition, Zaragoza-Cardiel et al. (2018) analyzed the SFR radial profile for 1027 star-forming complexes of 46 interacting galaxies and found that the SFR is clearly enhanced in the external parts far from the nucleus of galaxy pairs in intermediate-early stages of interaction.

In our previous works on H-KPAIRs (Xu et al. 2010; Cao et al. 2016; Domingue et al. 2016; Zuo et al. 2018; Lisenfeld et al. 2019), the results shown that spirals in S+E pairs have lower global sSFRs, SFEs, and interstellar radiation field intensities (dust temperatures) than that in S+S pairs (but comparable to that in isolated disk galaxies). We speculated that this is due to different mechanisms between S+S and S+E pairs in the interaction-induced star formation. The relatively higher star formation activities and lower gas-phase metallicities found in the off-nuclei regions in our two S+E pairs Arp142 and J0338+2120 also indicates that the star formation and gas inflow induced by galaxy interactions might be related to morphologies of the companions (spiral or elliptical). A larger sample (especially including more S+E pairs) is needed to make detailed studies on this topic and verify the results.

5. Summary

In this work, we carried out MOS observations on seven interacting galaxy pairs selected from the H-KPAIRs sample, using the 2.16 m telescope of Xinglong station, for studying their excitation mechanism, gas-phase metallicity gradients, and the distribution of star formation activities. The main results are as follows:

(1) The slopes (gradients) of the gas-phase oxygen metallicities (log(O/H)) for our interacting galaxy pairs are flatter than that in isolated disk galaxies, and the central metallicities of pairs are lower than normal spirals. This supports the predictions and results of previous theoretical numerical simulations and observational works which show the cold gas inflows induced by galaxy interactions can dilute the central metallicity.

(2) From the analysis of the radial distributions of SFR surface densities (Σ_{SFR}), we found that for galaxy pairs, the star formation occurs not only at galactic nuclei, but also in the off-nuclei regions, especially for two S+E pairs (Arp142 and J0338+2120). This suggests a dependence of star formation distributions for paired galaxies on their companion morphologies (Spiral or Elliptical), though we need a larger sample to verify this result.

In further works, we will enlarge the sample size and continue to make observations using MOS systems of Xinglong 2.16 m telescope and China Lijiang IFU (CHILI) on the Lijiang 2.4 m telescope, especially include more S+E pairs for studying their differences to S+S pairs. Also analysis of nearby interacting and merging galaxies by SDSS/MaNGA will be jointed to our MOS works to make comprehensive studies on the evolution of nearby interacting galaxies along the merging sequence.

We acknowledge the support of the staff of the Xinglong 2.16 m telescope. This work was partially supported by the Open Project Program of the Key Laboratory of Optical Astronomy, National Astronomical Observatories, Chinese Academy of Sciences. We acknowledge useful discussions with Dr. Yinan Zhu and Mr. Yun Wang. C.C. acknowledges support by the National Natural Science Foundation of China NSFC-11503013, NSFC-11420101002. H.W. and C.K. X. acknowledge support by the NSFC-11733006, NSFC-11873055, and the National Key R&D Program of China (No. 2017YFA0402704). This work is sponsored in part by the Chinese Academy of Sciences (CAS), through a grant to the CAS South America Center for Astronomy (CASSACA) in Santiago, Chile.

ORCID iDs

Bing-qing Zhang https://orcid.org/0000-0002-6659-1152
Zhi-min Zhou https://orcid.org/0000-0002-4135-0977

References

Baldwin, J. A., Phillips, M. M., & Terlevich, R. 1981, PASP, 93, 5
Barnes, J. E., & Hernquist, L. 1996, ApJ, 471, 115
Calzetti, D. 2001, PASP, 113, 1449
Cao, C., & Wu, H. 2007, AJ, 133, 1710
Cao, C., Xu, C. K., Domingue, D., et al. 2016, ApJS, 222, 16
Denicoló, G., Terlevich, R., & Terlevich, E. 2002, MNRAS, 330, 69
Domingue, D. L., Cao, C., Xu, C. K., et al. 2016, ApJ, 829, 78
Domingue, D. L., Xu, C. K., Jarrett, T. H., & Cheng, Y. 2009, ApJ, 695, 1559
Donzelli, C. J., & Pastoriza, M. G. 1997, ApJS, 111, 181
Ellison, S. L., Patton, D. R., Simard, L., & McConnachie, A. W. 2008, AJ, 135, 1877
Fan, Z., Wang, H., Jiang, X., et al. 2016, PASP, 128, 115005
Gavazzi, G., & Jaffe, W. 1985, ApJL, 294, L89
Kauffmann, G., Heckman, T. M., Tremonti, C., et al. 2003, MNRAS, 346, 1055
Kennicutt, R. C., Jr. 1998, ARA&A, 36, 189
Kennicutt, R. C., Jr., Bresolin, F., & Garnett, D. R. 2003, ApJ, 591, 801
Kennicutt, R. C., Jr., Keel, W. C., van der Hulst, J. M., Hummel, E., & Roettiger, K. A. 1987, AJ, 93, 1011

Kewley, L. J., Dopita, M. A., Sutherland, R. S., Heisler, C. A., & Trevena, J. 2001, ApJ, 556, 121
Kewley, L. J., & Ellison, S. L. 2008, ApJ, 681, 1183
Kewley, L. J., Geller, M. J., & Barton, E. J. 2006, AJ, 131, 2004
Kewley, L. J., Rupke, D., Zahid, H. J., Geller, M. J., & Barton, E. J. 2010, ApJL, 721, L48
Kovo, O., Beck, S. C., & Wolk, S. J. 1996, AJ, 111, 168
Liang, Y. C., Yin, S. Y., Hammer, F., et al. 2006, ApJ, 652, 257
Lisenfeld, U., Xu, C. K., Gao, Y., et al. 2019, A&A, 627, A107
Marino, R. A., Rosales-Ortega, F. F., Sánchez, S. F., et al. 2013, A&A, 559, A114
Michel-Dansac, L., Lambas, D. G., Alonso, M. S., & Tissera, P. 2008, MNRAS, 386, L82
Mihos, J. C., & Hernquist, L. 1996, ApJ, 464, 641
Moss, C., & Whittle, M. 1993, ApJL, 407, L17
Osterbrock, D. E. 1989, NYASA, 571, 99
Pettini, M., & Pagel, B. E. J. 2004, MNRAS, 348, L59
Powell, L. C., Bournaud, F., Chapon, D., & Teyssier, R. 2013, MNRAS, 434, 1028
Raimann, D., Storchi-Bergmann, T., Bica, E., Melnick, J., & Schmitt, H. 2000, MNRAS, 316, 559
Rupke, D. S. N., Kewley, L. J., & Chien, L.-H. 2010, ApJ, 723, 1255
Rupke, D. S. N., Veilleux, S., & Baker, A. J. 2008, ApJ, 674, 172
Smith, B. J., Soria, R., Struck, C., et al. 2014, AJ, 147, 60
Smith, B. J., Zaragoza-Cardiel, J., Struck, C., Olmsted, S., & Jones, K. 2016, AJ, 151, 63
Storchi-Bergmann, T., Calzetti, D., & Kinney, A. L. 1994, ApJ, 429, 572
Thronson, H. A., Jr., Hunter, D. A., Casey, S., Latter, W. B., & Harper, D. A. 1989, ApJ, 339, 803
Toomre, A., & Toomre, J. 1972, ApJ, 178, 623
Xu, C., & Sulentic, J. W. 1991, ApJ, 374, 407
Xu, C. K., Domingue, D., Cheng, Y.-W., et al. 2010, ApJ, 713, 330
Xu, C. K., Zhao, Y., Scoville, N., et al. 2012, ApJ, 747, 85
Zaragoza-Cardiel, J., Smith, B. J., Rosado, M., et al. 2018, ApJS, 234, 35
Zhou, Z.-M., Cao, C., Meng, X.-M., & Wu, H. 2011, AJ, 142, 38
Zhou, Z.-M., Wu, H., Huang, L., et al. 2014, RAA, 14, 1393
Zuo, P., Xu, C. K., Yun, M. S., et al. 2018, ApJS, 237, 2